Visualization of subsurface defects in composites using a focal plane array infrared camera

Yuri A. Plotnikov, William P. Winfree

NASA Langley Research Center, MS 231, Hampton, VA 23681-0001

ABSTRACT

A technique for enhanced defect visualization in composites via transient thermography is presented in this paper. The effort targets automated defect map construction for multiple defects located in the observed area. Experimental data were collected on composite panels of different thickness with square inclusions and flat bottom holes of different depth and orientation. The time evolution of the thermal response and spatial thermal profiles are analyzed. The pattern generated by carbon fibers and the vignetting effect of the focal plane array camera make defect visualization difficult. An improvement of the defect visibility is made by the pulse phase technique and the spatial background treatment. The relationship between a size of a defect and its reconstructed image is analyzed as well. The image processing technique for noise reduction is discussed.

Keywords: infrared thermography, image analysis, focal plane array detector, nondestructive evaluations

1. INTRODUCTION

Numerous experiments have demonstrated that infrared thermographic methods are effective for detection of subsurface flaws in graphite-epoxy composite materials. It is a promising technique for rapid large area inspection for a variety of defects: voids, inclusions, delaminations, porosity, and impact damages[1,2]. Periodic thermographic inspections of a structure during maintenance enable the monitoring of the growth of defects. High quality infrared imagers and powerful personal computers make the thermographic inspection very competitive and often the most rapid method for inspecting aerospace structures.

A new generation of infrared cameras with focal plane array (FPA) detectors provides a higher spatial resolution and improved sensitivity for near room temperature measurements, as compared to a scanned detector camera. These imagers are capable of faster full field data acquisition rates (hundreds of frames per second) and provide a high noise equivalent temperature difference (up to 0.025 $^{\circ}$C). Along with these advantages, the FPA cameras have an inherent disadvantage. The arrays consist of a large number of independent detectors that must be calibrated to yield accurate images of the radiance from the inspected component. Calibration requires the determination of an effective bias and gain for each of the individual detectors. Errors in the determination of the bias result in a persistent contribution to acquired thermograms or a vignetting effect. Errors in the determination of gain yield systematic noise to the pixel-to-pixel time variance between successive images.

The simplest application of active thermographic inspection consists of examining the thermal response of a structure at a fixed time following the thermal excitation. Improved detection of flaws is possible by measuring the temporal response of a structure to a thermal excitation. However, it is difficult to visually analyze a time series of thermal images. Therefore, analysis algorithms are required to extract the pertinent information from the time series and present it in one or two images for visual analysis. The development of these analysis techniques also offers the opportunity to reduce the effects of imperfect calibration of the focal plane arrays.

The purpose of this research is to develop a thermal data processing procedure capable of monitoring the growth of damage in an aerospace structure. These procedures extract the pertinent information from the time series of thermograms. At the same time, they reduce artifacts resulting from the array detector.

2. THERMAL IMAGE PROCESSING

2.1. Experimental procedure and visualization of the defects

To investigate effectiveness of different image processing procedures for defect visualization in composites, experiments have been performed on two pieces of graphite-epoxy composite polymer. One of them is from a thick stitched aircraft wing box structure. Five square flat bottom cavities have been fabricated in the backside of the specimen to various depths as sketched in Fig. 1. Two flash lamps induced a heat excitation in the front surface. The following cooling stage was monitored via an infrared imager with a 256x256 FPA *InSb* (Indium Antimonide) detector sensitive in the short wave band (3-5 μm). A series of 200 digitized images with 12 bit resolution produced by the camera with a sampling rate of 1 Hz was transferred into a personal computer for further image processing.
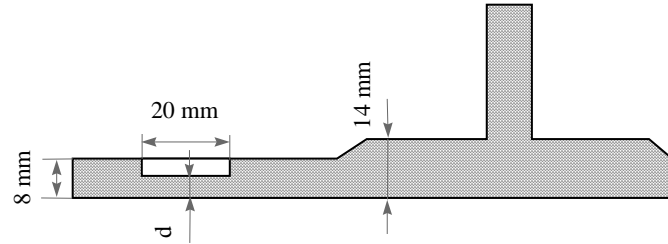

Figure 1. Flat bottom hole in the graphite-epoxy composite structure.

A background thermogram captured prior to heating is shown in Fig. 2a. The image covers a region of the panel 140x320 mm^2. The acquired thermogram of the panels' surface temperature appears hotter in the center, even though the surface has no spatial temperature variations (assuming the room temperature for the whole panel). The duration of the heat application (about 10 ms) is negligible compared to the heat diffusion process in the composite material and can be considered to be instantaneous. Unfortunately, the near surface structure of the panel dominates the thermal response immediately after flash. The through-the-thickness stitches produce dominant vertical lines in the thermal images for the first several seconds after heating. This pattern completely masks the presence of subsurface flaws in these images. A thermogram at 7 s after the flash is shown in Fig. 2b. The shallowest defect (2.0 mm below the surface) appears on this image. The paint marks on the surface and vertically oriented indications of stitches make interpretation of this image very difficult.
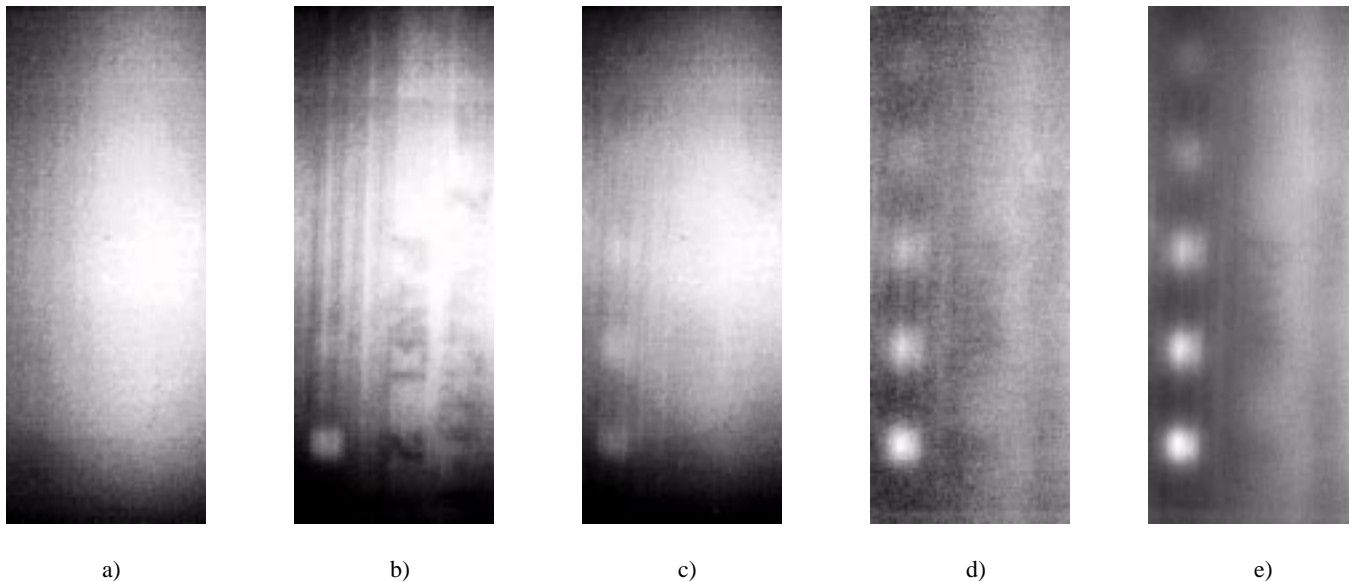

a)   b)   c)   d)   e)

Figure 2. Images of a composite panel with 5 square (20x20 mm^2) flat bottom cavities. The defects are located below the surface at depths of (from bottom to top): 2.0, 3.0, 4.1, 5.0, 5.3 mm. a) background image; b) thermal image at 7 s after the flash; c) thermal response averaged in the interval 10-50 s; d) thermal response averaged in the interval 10-50 s with the subtracted background; e) phase image.

Time averaging of successive thermal images yields an improved visualization of the defects located at the different depths and a higher signal to noise ratio. To determine the optimal time interval, the time evolution curves for the points located above the cavities and in a sound region were extracted from the collected images. The maximum of the thermal contrast for the defects located 2.0-5.3 mm below the surface occurs in the time interval from 15 to 45 s after the heat application. The thermal response of the surface averaged in the interval 10-50 s is presented in Fig. 2c. Indications of three square holes are recognized in the image. The stitches and surface marks are less visible. On the other hand, the systematic distortions are accumulated here. A histogram computed from this image is shown in Fig. 3a.

Subtraction of the thermogram taken before heating (Fig. 2a) results in a more uniform thermogram. The thermal response averaged in the time interval 10-50 s and modified in such a way is shown in Fig. 2d. It has been demonstrated[3] that a calibration procedure utilizing a linear function for each individual sensor can significantly improve quality of an FPA camera performance by reducing vignetting effect and noise. An internal calibration procedure can be performed on an FPA if the camera is equipped with a temperature reference source. Despite the fact that detector output is changing with temperature the subtraction of the background removes most of the artifacts. This is due to the relatively small temperature change of the panel caused by flash heating. The background subtracted image does not contain the bright area in the center any more. All five artificial defects can be localized in this image. The histogram of this image (Fig. 2d) has a lower median than the initial histogram with close to normal distribution.

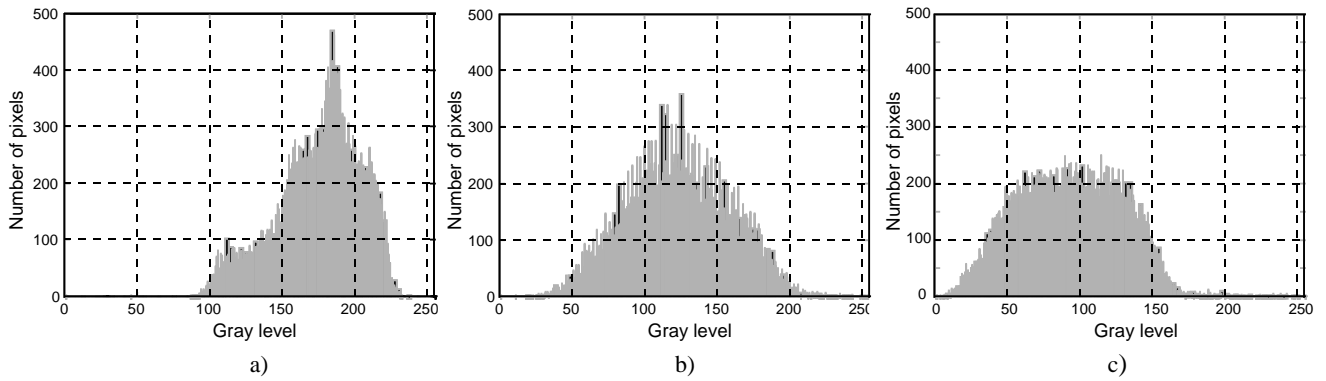|		
a)	b)	c)

Figure 3. Histograms computed from images Fig. 2c, 2d, and 2e respectively.

Line profiles above the defect centerline of the averaged thermograms before and after background subtraction are shown in Fig. 4. The plots were scaled to enhance comparison. The defects on the first profile are poorly visible due to high noise level and non-uniform background.
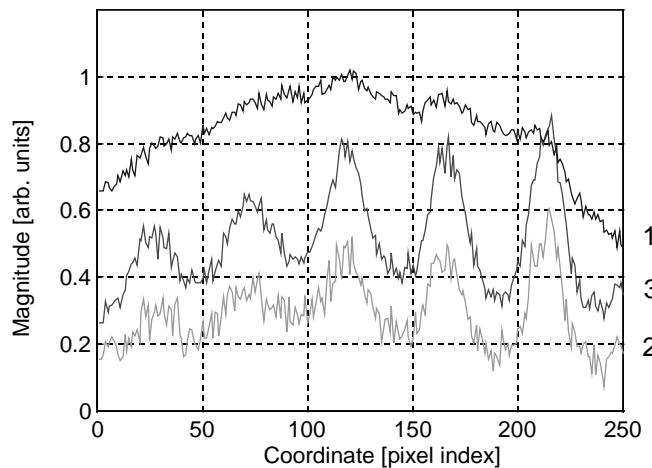

Figure 4. Profiles above the defect centerline. 1 - time-averaged thermal response; 2 - background subtracted thermogram; 3 - phase profile.

Improved defect visualization was obtained by applying the Discrete Fourier transform to the temporal thermal response curves extracted from the series of thermograms. The phase of the response at the fundamental frequency is calculated for each pixel using various time intervals[4]. Compared to the time averaging procedure, the pulse phase thermography requires a longer observation period. A phasegram shown in Fig. 2e was computed for the time interval 10-100 s after heating. The histogram of the phase image has a more homogenous pixel distribution (Fig. 3c). The profile obtained from the phase image demonstrates a higher sensitivity to the defects and a reduced noise level (Fig. 4, curve 3).

2.2. Emissivity problems

The tested structure has a very reflective surface. This decreases the amount of absorbed heat energy. Under the translucent epoxy coating, visible variations in the emissivity are apparent between the graphite fibers and stitches. This variation cause a non-uniform heat irradiation from the panel to the infrared imager. Coating of the surface with a high emissivity paint offers a possible solutions of this problem[1]. A 75 mm-tall upper portion of the panel (above the void located 5.3 mm under the surface) was painted black to investigate an improvement of defect visualization provided by the even emissivity. The difference between the coated and clear regions is most significant during the initial time following the heat application. With the heat diffuses into the specimen, the difference becomes less noticeable (Fig. 2b).

The noise levels in the painted and unpainted rectangles of equal sizes (95×70 mm^2) in the unflawed area of the specimen were compared. The mean and the standard deviation values computed from raw thermal images (m_T, σ_T), the time-averaged image (m_{Ta}, σ_{Ta}), the background subtracted thermogram (m_{Ta*}, σ_{Ta*}), and the phase image (m_ϕ σ_ϕ), are presented in Table 1. For the raw thermal images and in the time-averaged thermogram, the coat of paint results in a lower noise level (the standard deviation decreases from 0.88 % to 0.79 % and from 0.88 % to 0.60 % respectively). The time averaging with the background subtraction and the phase images do not have this trend. In fact, there is an increase of the σ_{Ta*} and σ_ϕ values in the coated region compared to the non-coated part. It is worth noting that the σ_{Ta} values are very close to the FPA camera noise level (the standard deviation in gray levels computed for a difference between two successive images is 0.83). The noise causes false calls for a defect detection procedure. This indicates that advanced thermal image processing experiences tend to reduce artifacts from emissivity variations. The stitches are more visible in the unpainted part in all acquired images. This indicates the stitches cause spatial variations in the thermal properties of the composite. Compensation for the inhomogeneities in the thermal properties is difficult. To date it has not been possible to remove all efforts of the stitching pattern with post processing. The paint coating still improves the defect visibility because it reduces the masking effect caused by stitches.

Table 1. Comparison of the noise level in painted and unpainted regions.

	Raw thermal image			Time averaging			Background subtracted			Phase image		
	m_T (gray level)	σ_T (gray level)	σ_T (%)	m_{Ta} (gray level)	σ_{Ta} (gray level)	σ_{Ta} (%)	m_{Ta*} (gray level)	σ_{Ta*} (gray level)	σ_{Ta*} (%)	m_ϕ (grad)	σ_ϕ (grad)	σ_ϕ (%)
Unpainted	774	6.81	0.88	759	6.69	0.88	8.76	1.25	14.3	12.2	1.97	16.2
Painted	788	6.23	0.79	769	4.60	0.60	9.86	1.56	15.8	13.2	2.39	18.1

3. LAPLACIAN-BASED DEFECT SHAPE EXTRACTION

An amplitude-based defect size extraction procedure can be applied to the images in Fig. 2d and 2e. For instance, the full width at half maximum of a spatial thermal profile above a subsurface defect can be used to compute the defect size[2]. However, such procedure requires preliminary determination of a sound area surrounding each defect. A less constrained approach to the defect sizing is based on a spatial gradient of the thermal response above a defect[5]. Application of the procedure to each line of a rectangular thermal image enables detection of multiple defects present in each image profile. A theoretical study has shown that this method provides an accurate defect size estimation along the major axes of an image when the defect has a lateral size greater than the thickness of the panel. However, it is difficult to apply this procedure to the thermal response directly because it requires a computation of the second spatial derivative. This significantly increases the noise and can produce distortions for defects whose orientation is different from the rectangular image grid.

A Laplacian-like two-dimensional filter gives improved results. The 7x7 element kernel is constructed to give a smoothed approximation to Laplacian of an image[6]. A convolution of the kernel and image is performed at an each point in the image. The kernel size is large enough to provide sensitivity to the spatial gradients with the orientations other than vertical or horizontal. Amplitude thresholding in the subsequent stage yields a binary defect map. This algorithm enables defect detection from a thermal image without prior information about the number of defects and their location. The threshold parameter controls the quality of the resulting defect map. Because the fiber structure causes non-homogeneous thermal images, if the threshold is too low, many small regions have the appearance of containing defect due to the fiber pattern. If the threshold is too high, a single defect has the appearance of being multiple smaller defects. An empirical rule for selection of the threshold was developed to enable detection of the maximum number of defects without a significant number of false calls.

The defect map in Fig. 5a was obtained from the time-averaged thermal response (Fig. 2c). It outlines the three defects located 2.0-4.0 mm under the surface and has the false calls indications caused by the stitches and paint marks on the panel's surface. A defect map computed from the background subtracted thermogram contains fewer false calls (Fig. 5b). It is possible to obtain continuous regions for the two deepest cavities by decreasing the threshold level. However, this dramatically increases the noise in the image. A defect map computed from the phasegram (Fig. 5c) has improved defect images as compared to the averaged thermogram and less false calls. It has been demonstrated[4] that a combination of two defect maps obtained by different methods provides a better quality of the defect appearance and with reduced noise. However, it is necessary to have images of all defects on both maps.
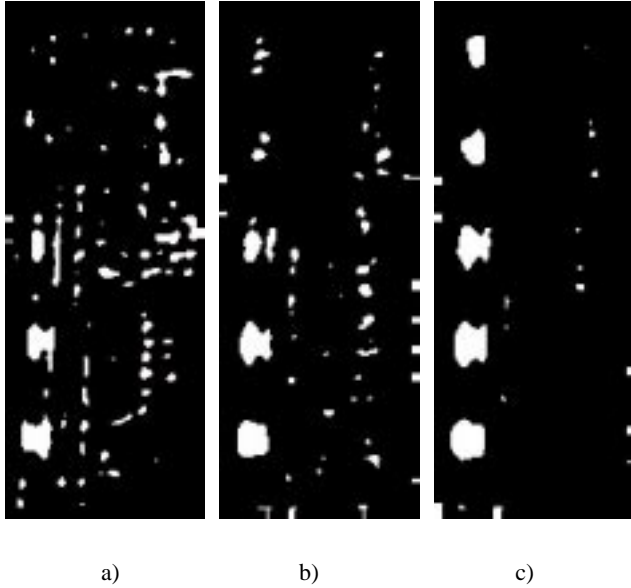

a)   b)   c)

Table 2. Defect size as it appears in the defect maps.

Def. depth [mm]	L_{hor} (thermal image)	L_{hor} (phase image)	L_{vert} (thermal image)	L_{vert} (phase image)
2.0	0.89	0.91	0.99	1.03
3.0	0.92	0.96	1.00	1.04
4.1	0.88	0.89	0.86	1.01
5.0	N/A	0.66	N/A	0.82
5.3	N/A	0.51	N/A	0.81

Figure 5. Results of image processing of the thermograms (a-b) and the phasegram (c).

The defect maps provide quantitative information about the lateral size of detected defects. Table 2 contains the size values of the defects obtained from both defect maps of Fig. 5b and Fig. 5c. The average detected vertical and horizontal sizes were normalized by the actual size of the defects (20 mm). The results demonstrate a good performance of the Laplacian-based shape extraction procedure. The difference between vertical and horizontal sizes is most likely a result of anisotropic thermal properties of the composite.

It is important that the defect map construction procedure be invariant to object rotation. Unknown defects may have different orientations relative to the image frame. Robustness of the described map construction technique was investigated by rotating a specimen having square artificial defects of different size and depth. A 3 mm thick graphite-epoxy composite panel with Nylon bagging film inclusions with 13, 19, 25, and 38 mm on a side was tested under the same conditions with a sampling rate of 15 Hz. The phasegram and defect map computed for the right angle orientation are shown in Fig. 6a-b. For a comparison, in Fig. 6c-d the phase image and defect map received on the rotated panel are presented. The boxed part in the

images contains the inserts located at the depth of 1.2 mm below the surface. The square shapes of the inclusions are visible in the both images.
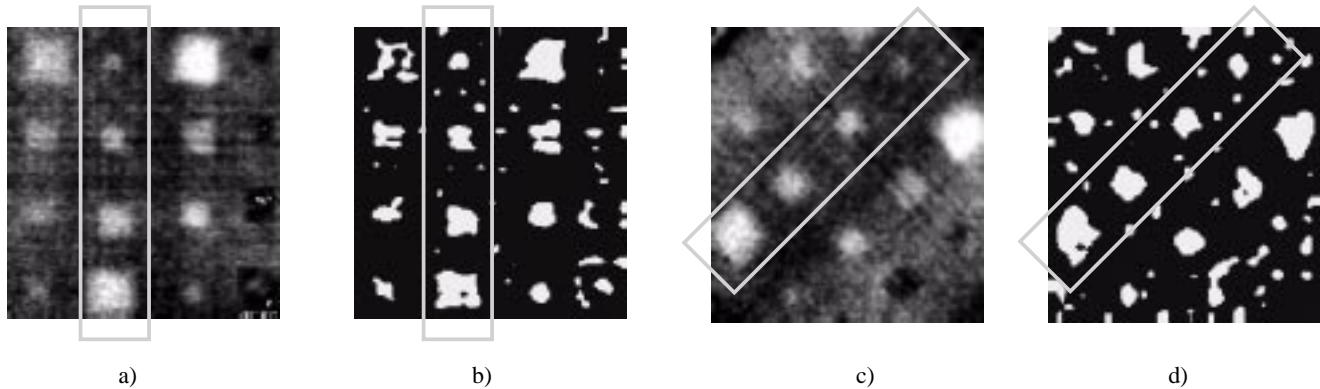

Figure 6. Effect of the object rotation. a) phasegram; b) defect map of the phasegram (a); c) phasegram of a rotated panel; d) defect map of the phasegram (c).

4. SUMMARY

This study has been done to improve quality of thermal images acquired via focal plane array infrared cameras. It has been shown that subtraction of a thermal image taken before heating significantly improves visibility of defects in a time-averaged thermogram. The phase image was found to give improved detectability of deep defects in the specimen when compared to the thermograms of the same specimen. A Laplacian-based defect shape extraction procedure demonstrates good performance and is suitable for quantitative analysis. The time-averaged thermograms and phasegrams can be used to monitor the growth of defects. It is planned to perform this analysis during a load testing of an aerospace component to verify its capabilities on more realistic aerospace structures.

ACKNOWLEDGMENTS

REFERENCES

1. J. L. Walker, S.S. Russel, G.L. Workman, "Thermographic Qualification of Graphite/Epoxy Instrumentation Racks," in: *Nondestructive Evaluation of Aging Aircraft, Airports, and Aerospace Hardware II*, G.A. Geithman, G.E. Georgeson, (Eds.), Proc. SPIE **3397**, pp. 141-148, SPIE, Bellingham, 1998.
2. D.P. Almond, P. Delpech, M.H. Beheshtey, and P. Wen, "Quantitative Determination of Impact Damage and Other Defects in Carbon Fiber Composites by Transient Thermography," in: *Nondestructive Evaluation of Materials and Composites*, Proc. SPIE **2944**, pp. 256-264, SPIE, Bellingham, 1996.
3. S. Marinetti, X. Maldague, and M. Prystay, "Calibration Procedure for Focal Plane Array Cameras and Noise Equivalent Material Loss for Quantitative Thermographic NDT", *Mater. Eval.* **55**, (3), pp. 407-412, 1997.
4. Plotnikov, W.P. Winfree, "Advanced Image Processing for Defect Visualization in Infrared Thermography," in: *Thermosense XX*, J.R. Snell, Jr. and R.N. Wurzbach, (Eds.), Proc. SPIE **3361**, pp. 331-338, SPIE, Bellingham, 1998.
5. Y.A. Plotnikov and W. P. Winfree, "Thermographic Imaging of Defects in Anisotropic Composites," in: *Review of Progress in QNDE*, D.O. Thompson and D.E. Chimenti (Eds.), **17A**, pp. 457-464, Plenum Press, New York, 1998.
6. W.P. Winfree, C.S. Welch, P.H. James, K.E. Cramer, "Thermographic Detection of Delaminations in Laminated Structures," in: *Review of progress in QNDE,* D.O. Thompson and D.E. Chimenti (Eds.), **8B**, pp. 1605-1612, Plenum Press, New York, 1989.